iScience

CellPress
OPEN ACCESS

Article

Confined assembly of ultrathin nanoporous nitrogen-doped graphene nanofilms with dual metal coordination chemistry

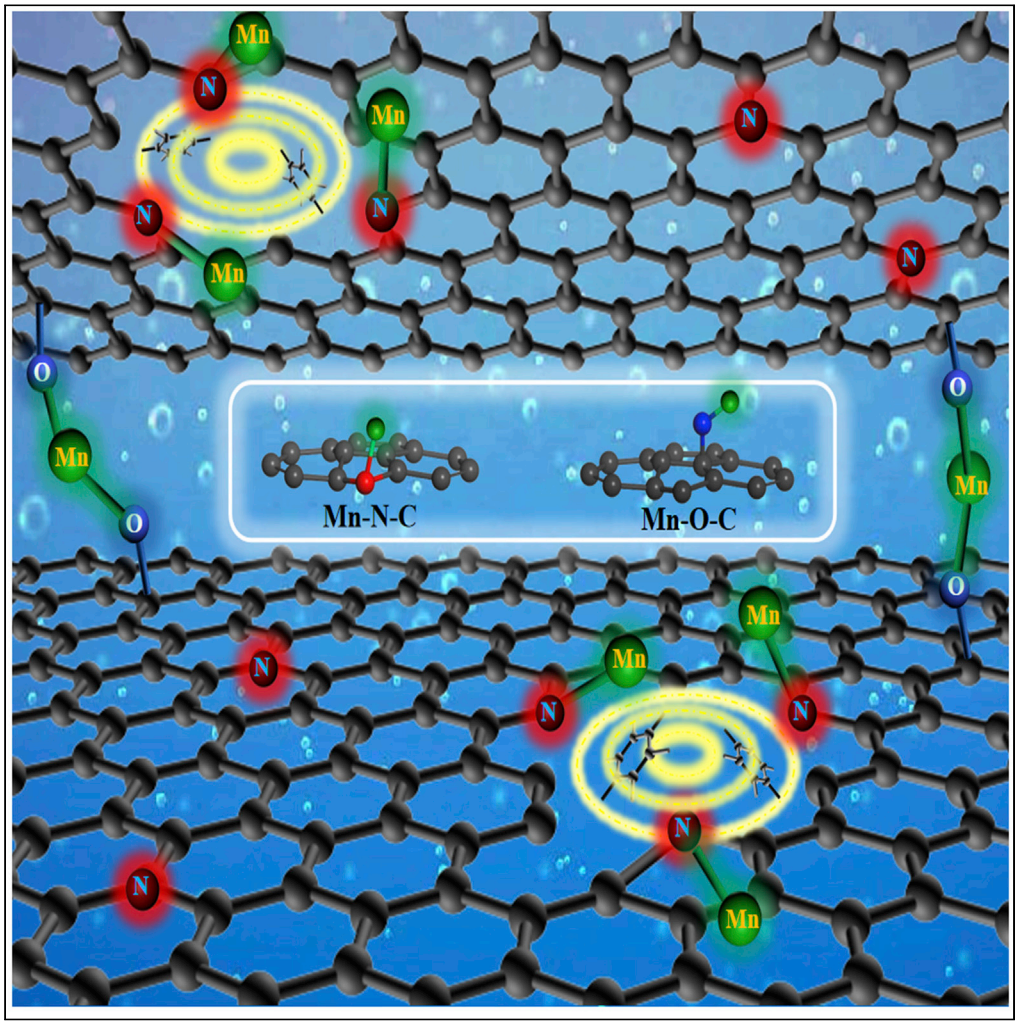

Zehai Xu, Yufan Zhang, Xu Zhang, ..., Yinghua Lu, Guoliang Zhang, Congjie Gao

guoliangz@zjut.edu.cn

Highlights

Dual metal-coordinated GO-based nanofilms are achieved by a general and facile method

Mn-N-C bonds are constructed in rGO nanosheets with N-containing coordinated links

Artificial nanopores are used to increase nanochannels for ultrafast mass transport

Generation of Mn-O-C bond greatly strengthens the stability of nanofilms in separation

Xu et al., iScience *24*, 102576
June 25, 2021
https://doi.org/10.1016/j.isci.2021.102576

iScience

CellPress
OPEN ACCESS

Article

Confined assembly of ultrathin nanoporous nitrogen-doped graphene nanofilms with dual metal coordination chemistry

Zehai Xu,[1,6] Yufan Zhang,[2,6] Xu Zhang,[1] Qin Meng,[3] Yujie Zhu,[1] Chong Shen,[3] Yinghua Lu,[4] Guoliang Zhang,[1,7,*] and Congjie Gao[1,5]

SUMMARY

Graphene oxide (GO) nanosheets with unique structure have received much attention in providing opportunity for high-performance membranes in separation. However, the rational design of ultrathin graphene membranes with controlled structures remains a big challenge. Here, we report a methodology to synthesize dual metal-coordinated ultrathin nanoporous graphene nanofilms by tailoring well-aligned nanocrystals as building blocks on heteroatom-doped GO nanosheets with tunable architectures. Manipulation of metal nitrate as bifunctional dopants realizes N-doping of graphene oxide and preferential growth of α-Mn_2O_3 nanocrystals. Generation of Mn-O-C bond during cross-linking greatly strengthens the stability of membranes for long-term steady operation. Meanwhile, because of spatial confinement effects and high binding energy, N-doped reduced GO nanosheets are desirable supports to construct numerous Mn-N-C bonds, thus generating artificial nanopores to significantly increase nanochannels for ultrafast mass transport. Moreover, the size-selective permeability of ultrathin nanoporous GO-based nanofilms can be optimized by managing the types of metal source for target coordination.

INTRODUCTION

Membrane technologies have attracted tremendous interests in recent decades and widely used in a range of commercial applications such as energy, biotechnology, drug delivery devices, petrochemical, and environmental industries (Park et al., 2017; Riley, 1991; Petersen 1993; Noble, 2006; Zhang and Koros, 2017). As the permeance and selectivity of membranes are principally determined by the film that manages the mass transport and solute rejection (Mi 2014; Fane et al., 2015; Zhang et al., 2019; Vankelecom 2002), design and control of structural characteristics of film play vital importance in improving the performance of membranes. Ultrathin nanofiltration membranes (<100 nm) are recently focused for their high permeation that is inversely proportional to thickness, the resistance of molecule transport through film can be minimized (Yang et al. 2017, 2019a, 2019b; Karan et al., 2015; Li et al., 2013; You et al., 2019). Nanofiltration membranes such as the Turing-type polyamide nanofiltration membranes with a thickness of 20 nm presented attractive characters in solution separation, specifically precise molecular sieving for small organic molecules and ions (Tan et al., 2018). Despite the rapid progresses that have been made, the rational design of ultrathin membranes with controlled structures remains a big challenge, and the current performance of ultrathin nanofiltration membranes is still not so high. The further development of nanostructured ultrathin nanofiltration membranes suitable for the highly efficient separation of small molecules is therefore of paramount importance.

On the basis of the unique atomic thickness, extraordinary physicochemical properties, and micrometer lateral dimensions, numerous attempts are made for providing the foundation in fabricating highly permeable graphene oxide (GO) membranes, which deposits a GO film on an ultrafiltration or a microfiltration membrane support (Mi 2014; Zhang et al. 2015, 2019; Yang et al. 2017, 2019a, 2019b; Li et al., 2013; Wang et al., 2019a; Wu et al., 2020; Song et al., 2017). Theoretical calculations showed that single-layered nanoporous GO membranes could achieve ultrafast molecule sieving (Cohen-Tanugi and Grossman, 2012). Encouraged by these results, many experimental works have been taken to synthesize ultrathin GO-based

[1]Center for Membrane and Water Science, Institute of Oceanic and Environmental Chemical Engineering, State Key Lab Breeding Base of Green Chemical Synthesis Technology, Zhejiang University of Technology, Hangzhou 310014, P. R. China

[2]College of Engineering, Carnegie Mellon University, Pittsburgh, PA 15213, USA

[3]College of Chemical and Biological Engineering, State Key Laboratory of Chemical Engineering, Zhejiang University, Hangzhou 310027, P. R. China

[4]College of Chemistry and Chemical Engineering, Xiamen University, Xiamen 361005, P. R. China

[5]Hangzhou Water Treatment Technology Development Center, National Engineering Research Center for Liquid Separation Membrane, Hangzhou 310012, China

[6]These authors contributed equally

[7]Lead contact

*Correspondence: guoliangz@zjut.edu.cn

https://doi.org/10.1016/j.isci.2021.102576

nanofiltration membranes for fast water purification. Unfortunately, compared with polymeric ultrathin membranes (Yang et al., 2017; Morelos et al., 2017; Fathizadeh et al., 2017; Xu et al., 2017), GO-based nanofiltration membranes with similar thickness displayed relatively low permeability owing to narrow channels. To solve this issue, the increase of interlayer spacing of GO layers was found to be an effective route to broaden nanochannels and facilitate the molecule transport during filtration process. However, because the introduction of extra functionalized molecules into interlayers of graphene nanosheets might increase the spacing distance to several nanometers, selectivity and stability degradation of GO membranes in separation inevitably occurred (Nam et al., 2016). Besides, overmuch intercalated additives hindered the transfer path of fluids, leading to low permeation through GO-based membranes. On these accounts, fabrication of GO-based ultrathin membranes by introducing artificial nanopores to create nanochannels may give opportunities to improve the permeance. By introducing nanopores, the permeability can be enhanced a lot, but nanoporous GO membranes usually display natural drawbacks of poor stability when hydrated (Morelos et al., 2017; Che-Ning Yeh et al., 2015). In addition, the structural integrity would be compromised owing to the generated nanopores. Therefore, the design of ultrathin GO-based nanofiltration membranes with high permeation and stability remains big challenging. So far, although the attempts including intercalation of macromolecules and introduction of nanopores have been explored between/inside the GO layers, there is no report on rational design of high-quality nanoporous GO-based membranes to obtain anticipated permeability through controlling coordination structures in interlayer confinement.

In view of these facts, here, we put forward the new idea of designing the process by which molecules swiftly permeate through such a metal-coordinated interlamellar network consolidated by functionalized GO and anisotropic nanocrystals. Because the construction of reliable ultrathin GO-based nanofiltration membranes in microscopic confined spaces of two-dimensional nanomaterials faces some great challenges including thickness adjustment of the film, distribution of uniform and narrow nanopores, and improvement of mechanical strength, before ultrathin GO-based membranes will be put into use on a wide scale, at least the exemplary settlement between molecular sieving and the mechanism that rationalizes the formation of efficient and stable ultrathin GO-based membranes should be outlined. In this work, we have discovered that the manipulation of metal nitrate as bifunctional dopants realized N-doping of graphene oxide and simultaneously controlled anisotropic growth of α-Mn_2O_3 nanocrystals. More importantly, the chemical coordination between N-doped GO nanosheets and multivalent cations resulted in the generation of Mn-N-C bonds so as to create numerous artificial nanopores. This unique structure greatly broadened the nanochannels with ultralow friction for fluid permeation. The nanoporous Mn/N-rGO films created from metal-coordinated N-doped GO with controllable thickness down to a nanometer scale achieved prominent permeance. Furthermore, the size-selective permeability of ultrathin nanoporous GO-based nanofilms can be adjusted by varying the types of metal source for target coordination.

We report a methodology for synthesizing dual metal-coordinated ultrathin nanoporous GO-based nanofilms with size selectivity at a molecular scale by assembling anisotropic Mn_2O_3 nanocrystals channeled N-doped reduced-GO nanosheets (Mn/N-rGO) on polylevodopa (PLDA)-coated polymer supports, which were highly stable in cross-flow nanofiltration (Figures 1A–1H). Narrow dispersed GO nanosheets were initially achieved by multiple centrifugation and ultrasonic treatment (Figure 1A). The thickness of prepared stable ultrathin GO nanosheets with several micrometers in size is around 1.52 nm measured by atomic force microscopy (AFM) (Figures 1I and 1J), revealing the existence of few-layered GO (Shen et al., 2016). The intrinsic negative charge of carboxyl units on GO nanosheets makes them good candidates to fabricate robust nanocomposites by assembling with positively charged manganese oxide nanocrystals. After introducing manganous nitrate as a precursor into GO suspension with reductant $NaBH_4$, GO nanosheets were reduced to rGO and doped with N element (Figures 1B and 1C). Meanwhile, N-doping of rGO can supply stronger synergetic chemical coupling between rGO nanosheets and Mn species. The heteroatoms doping in rGO nanosheets acted as nucleation sites for anchoring of nanocrystals, thus promotd Mn_2O_3 nanocrystals growing on the rGO surface as well as simultaneous cross-linking with rGO nanosheets (Figure 1D). The prepared mixed-dimensional Mn/N-rGO hybrids display an interconnected porous framework of N-doped rGO sheets with highly uniform deposition of Mn_2O_3 nanocrystals evidenced by energy dispersive spectrometer analysis (Figure 1K). We immersed a polysulfone (PSF) support into a PLDA bath and dried it at room temperature (Figures 1E and 1F). The novel Mn/N-rGO nanofilms assembled on PLDA/PSF substrate in a facile synchronous filtration process (Figures 1G and 1H), which can be folded completely without breakage (Figure S1).

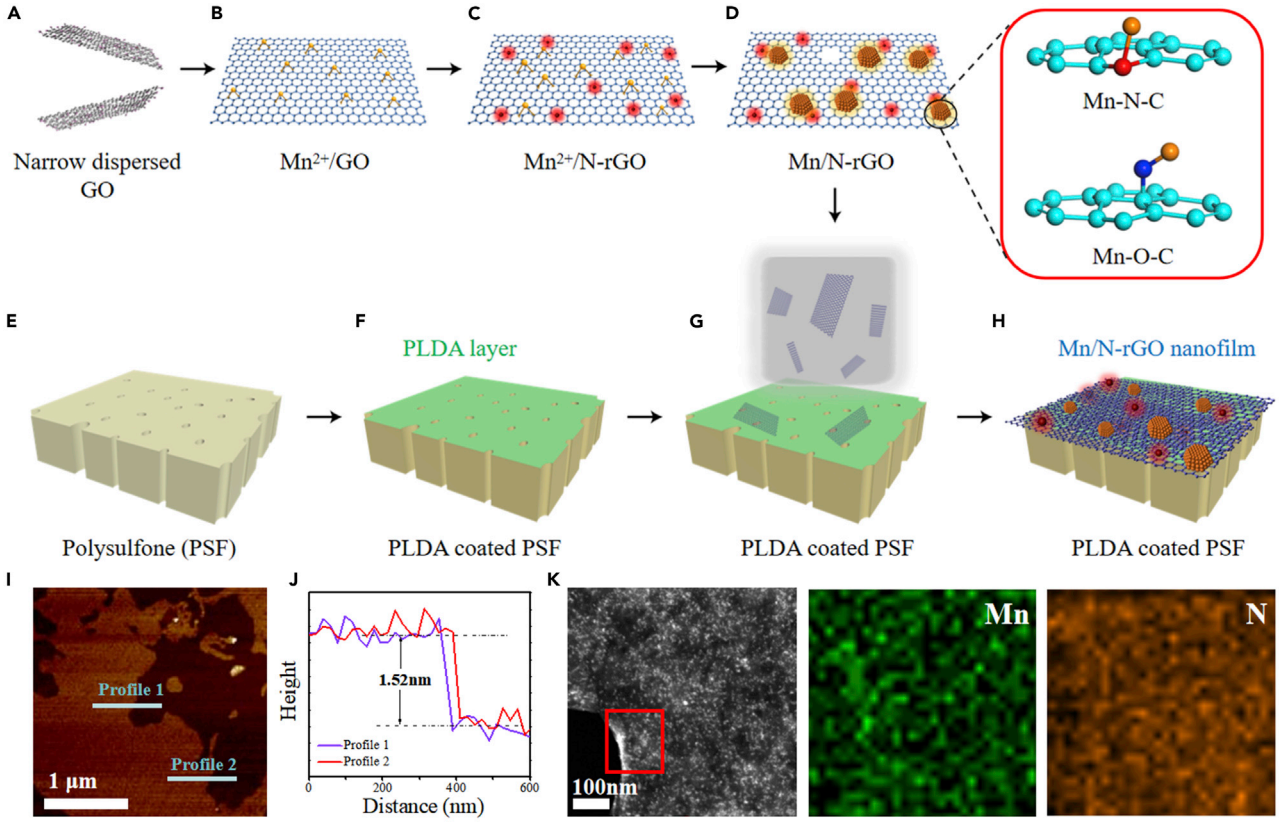

Figure 1. Confined assembly of dual-metal-coordinated ultrathin Mn/N-rGO nanofilms

(A) Narrow dispersed GO nanosheets.

(B) Mn^{2+}/GO nanosheets by cross-linking.

(C) N-doped Mn^{2+}/N-rGO nanosheets.

(D) Nanoporous Mn/N-rGO nanosheets with two kinds of coordination structures (Mn-N-C and Mn-O-C).

(E) Porous polysulfone support.

(F) PLDA later coating on the PSF support.

(G) The Mn/N-rGO solution is deposited on the surface of PLDA-coated PSF support.

(H) Synthesized nanofiltration membrane with ultrathin Mn/N-rGO nanofilm. As per the contents of GO and Mn in casting solution, Mn/N-rGO nanofilms on LDA/PSF substrate are labeled as GCN-1, GCN-2, GCN-3, and GCN-4 membranes, respectively.

(I and J) AFM image and corresponding height profiles of GO nanosheets.

(K) Element mapping of Mn/N-rGO composites.

RESULTS AND DISCUSSION

Because a local coordination environment greatly influences the properties of metal-coordinated compounds, manipulation of metal centers and surrounding coordination atoms can effectively improve the physicochemical properties. In conventional metal/GO composite membranes, metals coordinated with GO by forming a single metal-oxygen bonding to stabilize GO layer in water. In our design, we first explored two different manganese sources (manganese sulfate and manganese acetate) to synthesize Mn/rGO composites with a single coordination environment. The synthesized single-metal-coordinated Mn/rGO nanofilms showed acceptable size-selective permeability and good stability during cross-flow nanofiltration. After that, we introduced N atoms to dope GO nanosheets to obtain different chemical binding (C-N bonds and triazine rings). Meanwhile, a new coordination environment was applied to generate two kinds of coordination structures (Mn-N-C and Mn-O-C) and dual-metal-coordinated Mn/N-rGO nanofilms were successfully achieved. It was found that N-coordination in metal/GO compounds obviously altered the strength of metal-oxygen bonding and improved the electron-donor properties. Very different from conventional metal-coordinated N-doped carbon compounds, our metal/N-rGO building blocks were created via a facile and low-cost one-step method for the first time, no need for high-temperature pyrolysis. Interestingly, we also discovered that the N-doping strategy of rGO nanosheets

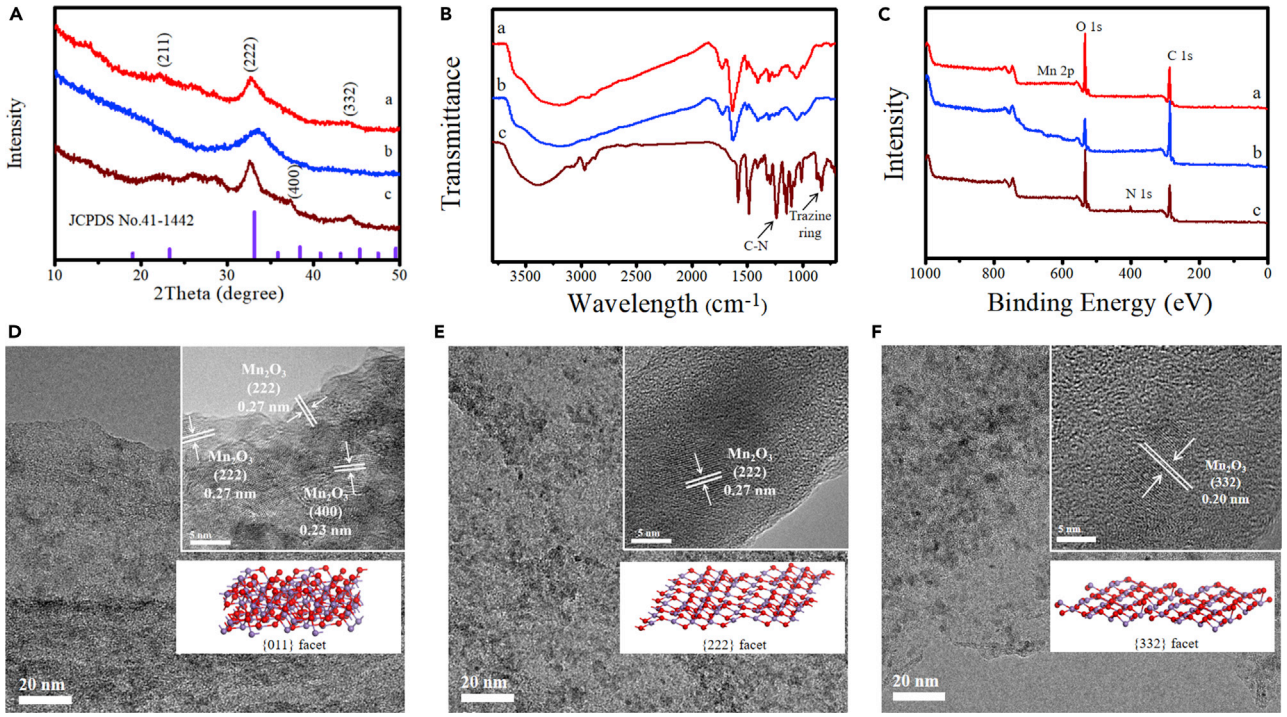

Figure 2. Metal-coordinated building blocks of single- and dual-metal-coordinated ultrathin nanofilms

(A–C) XRD patterns, FTIR spectra and XPS spectra of synthesized Mn/rGO building blocks from dual-metal-coordinated nanofilms (A) and single-metal-coordinated nanofilms (B and C). TEM and HRTEM image of Mn/rGO building blocks from single-metal-coordinated nanofilms (D and E) and dual-metal-coordinated nanofilms (F).

significantly contributed to induce the preferred growth of Mn_2O_3 nanocrystals, which can be deduced from the intensity ratio of different facets. The value of intensity ratio of (332)/(222) was 0.21, which was greater than the standard (0.11) (JCPDS No. 41-1442), indicating the orientation along the (332) facet was preferred (Figure 2A), in agreement with HRTEM analysis (Figure 2F). Consistent with expectations, the generated Mn_2O_3 nanocrystals on undoped rGO (Figures 2B and 2C) by using manganese sulfate and manganese acetate as precursors only exposed {011} and {222} facet, respectively (Figures 2D and 2E). Nanoparticle with specific crystal facet possessed high density of atomic steps, ledge adatoms, terraces, and kinks, which served as active sites for breaking chemical bonds, thus generating abundant nanopores in GO nanosheets by coordination-aided chemical etching. Manipulating the types and characters of metal centers and corresponding coordination atoms may leads to extended applications given that these variables can greatly impact certain properties of nanoporous materials.

The composition and structure control of membranes provides a good opportunity to improve the physicochemical properties and increase its separation efficiency (Shannon et al., 2008; Yang et al. 2019a, 2019b; Wang et al., 2019c; Zhao et al., 2018). To confirm the tunable structures of dual-metal-coordinated ultrathin membranes, we initially focused on the composition of prepared samples. As depicted in Figure 3A, the content of Mn could be linearly increased by adding more precursors, but the concentration of nitrogen no longer changed when the precursor went up to 25 mmol/L. After metal precursors were introduced, *in situ* generated Mn_2O_3 nanocrystals with a mean size in the range of 3.87–5.40 nm grown on N-rGO nanosheets were observed (Figure S2). The thickness of nanofilms and particle size of Mn can be rationally controlled by adjusting the concentration of metal precursors (Figure 3B and Table S1). The Mn/N-rGO nanofilm of GCN-1 membrane with rGO loading of 28 mg/m^2 possessed a very small thickness down to 38.8 $\pm$ 2.7 nm (Figures 3E and 3F). Meanwhile, the thickness of nanofilm in GCN-4 membrane maximally reached 65.1 $\pm$ 5.2 nm when the particle size approached 5.40 nm (Figures 3K and 3L), still fell within the ultrathin scope of graphene-based membranes. Different from reported membranes with a very thick film, the sharp decrease in thickness of as-prepared Mn/N-rGO nanofilms effectively reduced the resistance of mass transport through the film, thus greatly enhancing the permeance in separation. With Mn ions cross-linking N-doped rGO nanosheets, Young's modulus and hardness were improved from

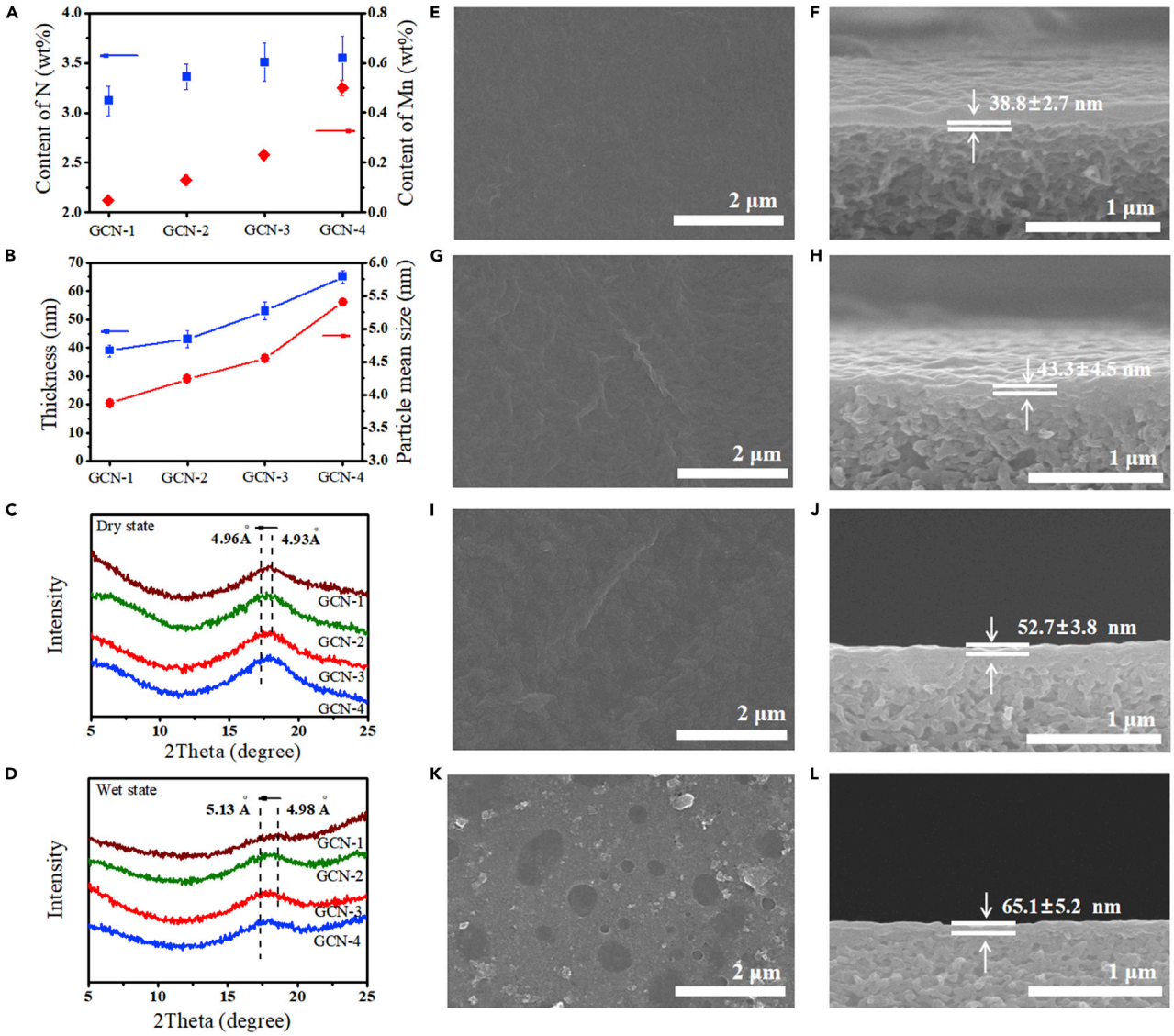

Figure 3. Morphology, composition, and structure control of dual-metal-coordinated ultrathin Mn/N-rGO nanofilms

(A) Content of nitrogen and manganese determined by XPS.

(B) Thickness of prepared Mn/N-rGO nanofilms and mean size of Mn_2O_3 nanoparticles in different membranes.

(C–L)(C and D) XRD patterns of Mn/N-rGO nanofilms in dry state and wet state. Surface and cross-section SEM images of different ultrathin Mn/N-rGO nanofilms: (E and F) GCN-1 membrane; (G and H) GCN-2 membrane; (I and J) GCN-3 membrane; and (K and L) GCN-3 membrane. Data are represented as mean ± SEM.

3.19 ± 0.67 to 9.27 ± 1.39 Gpa and 0.28 ± 0.05 to 1.75 ± 0.11 Gpa, which was 3 times and 2.3 times higher than that of GCN-0 membrane and other reported GO-polymer membrane (Ko et al., 2015), respectively. Through using appropriate content of fillers, the mechanical properties of Mn/N-rGO nanofilms can be controlled flexibly and resulting excellent stability can be applied to deal with aggressive cross-flow situations. To demonstrate the universality of our strategy, we also used other metal nitrate as precursors and controlled their contents to prepare other dual-metal-coordinated ultrathin metal/N-doped rGO nanofiltration membranes, such as Fe/N-rGO and Co/N-rGO nanofilms (Figure S3), which not only possessed high mechanical stability but also held satisfactory selective permeability.

As per the nature of graphene-based membrane, the subnanometer level mechanism of interlayer spacing control proves to be pivotal in defining the terminal mass transfer of fluid systems (Zhang et al., 2020). We

found that the intercalation of Mn_2O_3 nanocrystals into the N-rGO nanofilms not only inhibited the restacking of N-rGO nanosheets but also created well-defined nanochannels within Mn/N-rGO nanofilms. XRD results demonstrate that the d-spacing of pure GO membrane was 9.30 Å, while the distance of N-rGO nanofilm decreased to 5.05 Å after the reduction when the concentration of Mn was adjusted at 25 mmol/L in the wet state (Figure 3D). However, smaller d-spacing could be obtained with further enlarging the Mn content in Mn/N-rGO nanofilms. The spacing expanded from 4.93 Å to 4.96 Å in the dry state (Figure 3C) and increased from 4.98 Å to 5.13 Å in the wet state when the concentration of Mn reached 0.05 mmol/L. Nevertheless, the Mn/N-rGO nanofilms still exhibited high antiswelling capacity and compact structures in water; in which, the maximum swelling distance of Mn/N-rGO nanofilm in GCN-4 membrane was only 0.2 Å in water, much less than that of other reported GO/polymer membranes (2.5 Å) (Xu et al., 2016).

Because separation behaviors of different membranes were principally determined by the film that manages both mass transfer and solute rejection, creation of ultrathin membranes with potentially high permeance and selectivity has become the current new hot point (Yang et al. 2017, 2019a, 2019b; Karan et al., 2015; Li et al., 2013; You et al., 2019). Our design of Mn/N-rGO nanofilms with nanoscale ultrathin separating nanofilms enabled water molecules to pass through the nanochannels of membranes under very low resistance. Abundant artificial nanopores in Mn/N-rGO nanosheets were facilely formed after formation of Mn-N coordination structure, thus providing unimpeded pathways for ultrafast water transport. Simultaneously, the targeted solute molecules were easily separated with very high selectivity, further endowing the nanochannels of membranes with ultralow friction. In addition, because N-doped rGO served as favorable nucleation and anchor sites for generating anisotropic Mn_2O_3 nanocrystals, the strong interactions between N-doped rGO nanosheets and Mn_2O_3 nanocrystals greatly promoted the formation of C-O-Mn bond so as to fix Mn_2O_3 nanocrystals and strengthen the stability of membranes for long-term operation. In the testing experiment, different kinds of Mn/N-rGO nanofilms were tested to evaluate the permeability in cross-flow nanofiltration under low pressure of 1.0 bar, in which Naphthol green B (NgB) was selected as target solute. Compared with original rGO membrane without metal coordination (3.01 L m^{-2} h^{-1} bar^{-1}, 99.5% for NgB), single-metal-coordinated Mn/rGO nanofilms by using manganese sulfate as a precursor (107.5 L m^{-2} h^{-1} bar^{-1}, 99.5% for NgB), and manganese acetate as a precursor (98.7 L m^{-2} h^{-1} bar^{-1}, 99.7% for NgB) (Figure S4), all the prepared ultrathin Mn/N-rGO nanofilms with dual-metal-coordination exhibited significantly higher permeate flux owing to the fact that intercalation of Mn between the N-rGO layers generated large quantities of nanochannels inside membranes. Among these membranes, the ultrathin GCN-3 membrane (53 nm) displayed a significantly high water permeance of 210 L m^{-2} h^{-1} bar^{-1} together with satisfactory rejection of 99.8% for NgB, surpassing most previously reported GO-based and polymeric ultrathin membranes with thickness lower than 100 nm for water purification (Figure 4A and Table S2) (Yang et al. 2019a, 2019b; Morelos et al., 2017; Xu et al., 2019; Wang et al., 2019b; Nam et al., 2019; Liu et al., 2019; Soyekwo et al., 2017; Lin et al., 2018; Shen et al., 2019; You et al., 2019). To further determine the ultrafast molecular sieving properties of ultrathin nanofiltration membranes, dye molecules with different sizes and charges were used as molecular probes to characterize the selectivity owing to their easy detection, good solubility, and broad choice. Because the Mn/N-rGO nanofilm was negatively charged (Figure S5), the prepared membranes showed almost no rejection to positively charged molecules (MnB). The rejection rates of negatively charged dyes in GCN-3 membrane reduced sequentially with molecular size of dyes (Figures 4B and S6) (100% for EB [3.4 nm], 99.8% for NgB [2.4 nm], 98.8% for MB [2.3 nm], 98.5% for CR [2.2 nm], 98.6% for MG [2.0 nm], 76.2% for X-3B [1.6 nm], 67.5% for RB [1.6 nm] and 52.5% for MO [1.2 nm]). The fluid pathway in GCN-3 membrane was wider than the size of X-3B but narrower than the size of CR, indicating good size-selectivity at a molecular scale (Li et al. 2016a, 2016b). Therefore, we deduced that the size of nanochannels should be in the range of 1.6–2.0 nm, which were wide enough for four to five layers of water molecules transport between Mn/N-rGO layers to achieve high water permeance.

Across the library of ultrathin membranes, we learn that a key point in designing the basic coupling system is how to keep the balance between structural stability and separation efficiency. By investigating the separation behaviors of GCN-3 membrane at a cross-flow rate of 120 L h^{-1} for a long period continuous operation of 5 cycles, we observed that the permeate flux of GCN-3 membrane showed little fluctuation of permeate flux for at least 100 h, while the rejection rate for NgB was kept stable as high as 97.0% for the whole period (Figure 4C), displaying prominent stability. For comparison, single-metal-coordinated Mn/rGO nanofilms by using manganese sulfate and manganese acetate as a precursor remained a

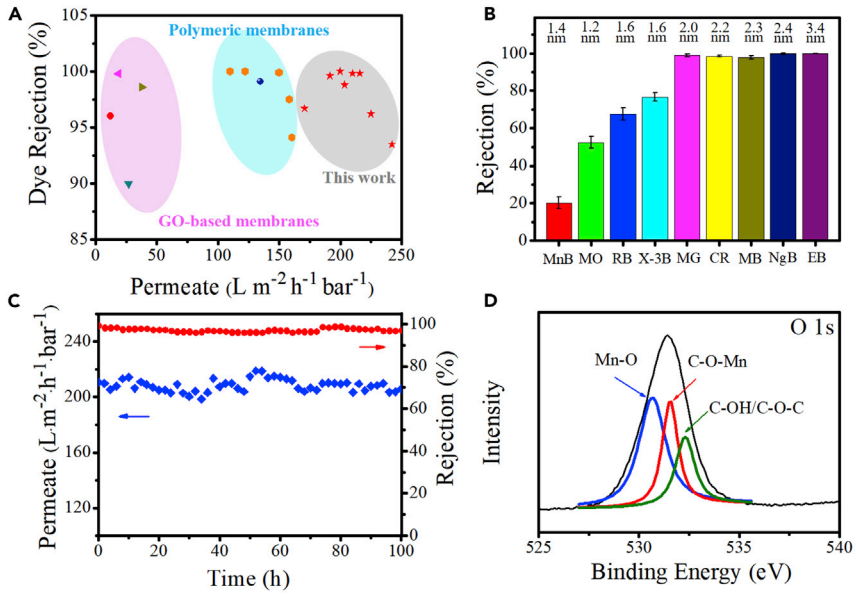

Figure 4. Separation behaviors of dual-metal-coordinated ultrathin Mn/N-rGO nanofilms

(A) Separation performance of state-of-the-art ultrathin GO-based and polymeric membranes with thickness lower than 100 nm for water purification in literatures. Red sphere: GO/FLG; green triangle: GO/PC; pink triangle: PGO; green brown triangle: mil-EGO; orange hexagon: MOPM-Fe^{3+}/PAN; blue sphere: SCOF/PDA-PAN; red pentacle: Mn/N-rGO.

(B) Rejection of several dyes in water versus molecular size. The dyes used: methylene blue (MnB), methyl orange (MO), rhodamine B (RB), reactive brilliant red X-3B, methyl green (MG), congo red (CR), methyl blue (MB), NgB and evans blue (EB). Data are represented as mean +/−.

(C) Performance of GCN-3 membrane in long-term continuous separation.

(D) XPS spectrum of O 1s peaks for GCN-3 membrane.

continuous operation for 56 h and 62 h, respectively. To stress the stability of Mn/N-rGO nanofilms more directly, we soaked both prepared membranes in water at a wide pH range for a period of time. Pure GO membrane was disintegrated instantly when hydrated and totally redispersed after only 1 h; however, Mn/N-rGO nanofilms kept structure integrity for at least 90 days (Figure S7), superior to extraordinary stability of the reported GO composite membrane that can be maintained in water for one month. Through regulating the introduced contents of Mn_2O_3 nanocrystals, the nanofilms were highly stable in water because of the cross-linking between Mn ions and N-doped rGO nanosheets and the formation of Mn-O-C bond, which was evidenced by the X-ray photoelectron spectroscopy (XPS) analysis (Figure 4D). More importantly, such strong interactions between N-doped rGO nanosheets and Mn_2O_3 nanocrystals greatly promoted Mn/N-rGO nanofilms keeping structural integrity even under sonication (50 KHz) for at least 1 h, which is a very long operation period for graphene-based membranes. Comparatively, the Mn/rGO nanofilm as parallel easily disorganized under same sonication after only very short 54 s. To evaluate the stability in applicable conditions, the filtration experiments at pH range of 8–10 were carried out. Although the permeance of GCN-3 membrane was slightly decreased owing to the precipitation of $Mn(OH)_2$, the GCN-3 membrane remained with a high permeance of 205.6 L m^{-2} h^{-1} bar^{-1} and high rejection (99.8%) toward small organic molecules. Moreover, the concentration of Mn ions leached from GCN-3 membrane (7.065 cm^2) was only 0.01 mg/L, which was lower than the drinking water standards (0.05 mg/L) (Figure S8). Besides the aforementioned features, the most noticeable difference with other reported membranes lies in the antifouling ability during nanofiltration. Because of the introduction of hydrophilic Mn_2O_3 nanocrystals, the hydrophilicity of prepared Mn/N-rGO nanofilms was obviously enhanced (Figure S9), endowing the membrane with improved fouling-resistant ability (Sun et al., 2019; Ma et al., 2019). The as-synthesized Mn/N-rGO nanofilms exhibited high fouling resistance with negligible flux decay for at least 100 h.

To explicate the high performance of ultrathin Mn/N-rGO nanofilms in fluid separation, we used molecular dynamics (MD) simulations to verify the interactions between N-doped nanosheets and Mn_2O_3 nanocrystals. The length of Mn-quaternary N is 2.88 Å (Figure 5A), demonstrating that the interaction between

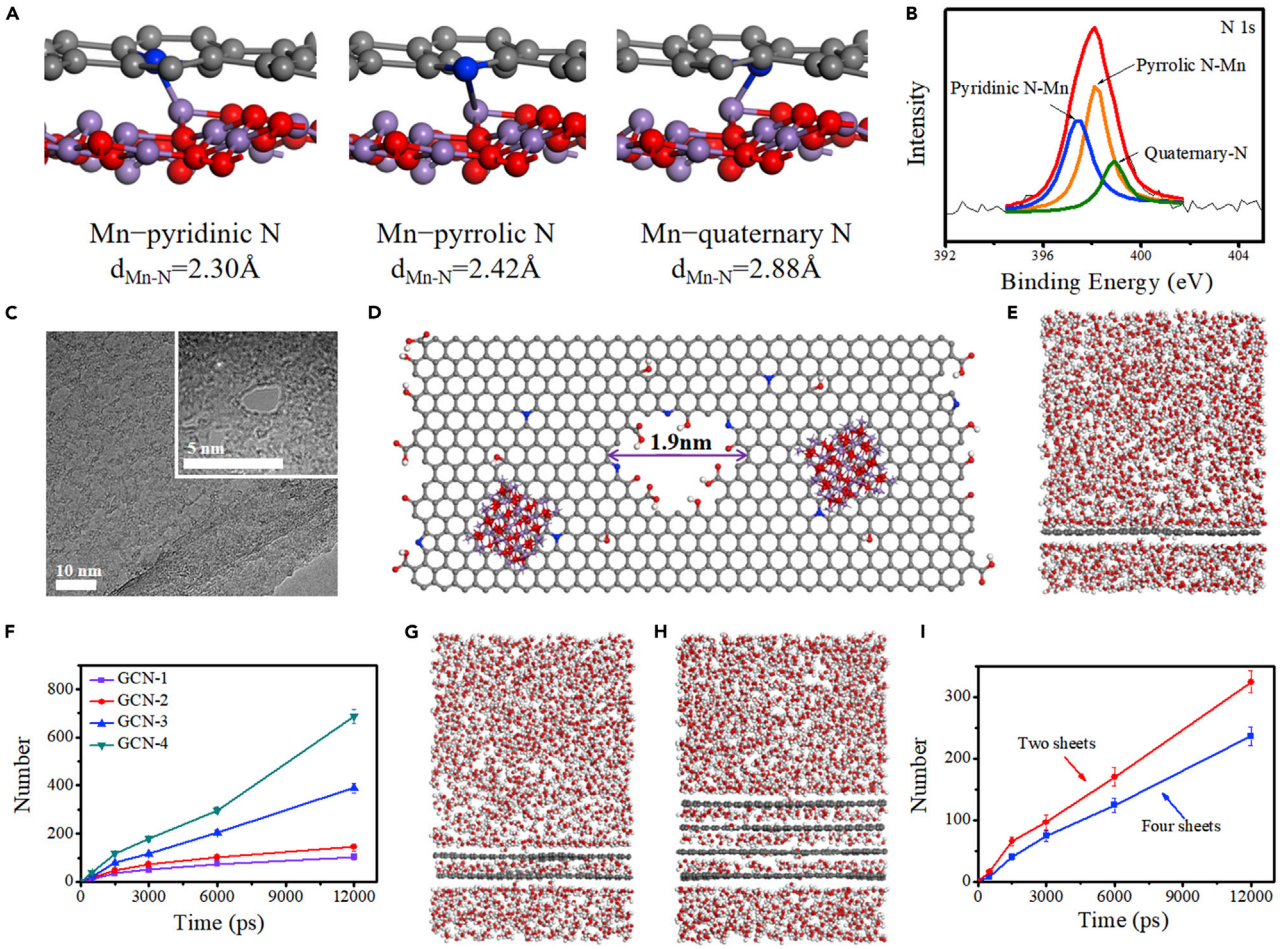

Figure 5. Molecular dynamics simulations

(A) Bond lengths of Mn-pyridinic N, Mn-pyrroloc N and Mn-quaternary N. Gray sphere: C, blue sphere: N, red sphere: O, purple sphere: Mn.

(B) XPS spectra of N 1s for GCN-3 membrane.

(C) HRTEM images showing the nanopores of Mn/N-rGO nanosheet in GCN-3 sample.

(D) Snapshots of the MD simulation systems top view of the Mn/N-rGO nanosheet with an artificial nanopore (1.9 nm). C, O, N and H atoms were drawn as cyan, red, blue and white spheres, respectively.

(E, G, H) Snapshots of the MD simulation systems of water flowing through single-layered Mn/N-rGO, double-layered Mn/N-rGO, and four-layered Mn/N-rGO.

(F) Number of water molecules flowing through different single-layered GCN membranes.

(I) Number of water molecules flowing through double-layered Mn/N-rGO and four-layered Mn/N-rGO as a function of simulation time. Data are represented as mean +/−.

quaternary N and Mn was pretty weak. On the contrary, the length of Mn-pyridinic N and Mn-pyrroloc N bonds was 2.30 Å and 2.42 Å, respectively, revealing strong chemical interactions between pyrrolic/pyridinic N and Mn_2O_3 nanocrystals (Yu et al., 2019), which is in agreement with the XPS analysis (Figure 5B). Based on the results of HRTEM, XPS and Fourier transform infrared spectrometer (FTIR) analysis (Figures 5C, S10, and S11), we found that many artificial nanopores were generated after the formation of Mn-N coordination structures by coordination-aided chemical etching, therefore we established physical models (Mn/N-rGO nanosheets with different artificial nanopores) to investigate molecular permeation of water passing through Mn/N-rGO composite nanochannels (Figure 5D). Different ultrathin Mn/N-rGO nanofilms were filled with water in the simulation box with the Forcite module, yielding a simulation model containing 2000 molecules. We suppose that water molecules exhibit high diffusion in Mn/N-rGO owing to the artificial nanopores and interlayer spacing distance. The simulations demonstrate that water molecules pass through a Mn/N-rGO nanosheet with a 1.9-nm pore when compared with that of models with a small pore for GCN-1 and GCN-2 samples, and the flux of a single-layered Mn/N-rGO nanosheet in GCN-3

sample is 32.4 molecules ns^{-1} for water (Figures 5E and 5F). Although the GCN-4 sample obtains a higher flux of 57.3 molecules ns^{-1}, effective rejection for small molecules will not be achieved owing to the larger pore (5.9 nm). To further prove the high flow velocity in thick separation films, the MD simulations of the GCN-3 membrane with different layers were displayed (Figures 5G and 5H). The flow velocity of water through double-layered (27.0 molecules ns^{-1}) and four-layered (19.7 molecules ns^{-1}) Mn/N-rGO nanosheets is very close to that of a single-layered sample (Figure 5I), revealing that water molecules can preferentially pass through artificial nanopores with ultralow friction (Wang et al., 2017), thus promoting the mobility of water molecules and obtaining high water flux.

Conclusion

In conclusion, we report a general and facile strategy to design and synthesize dual-metal-coordinated ultrathin nanoporous GO-based nanofilms by assembling anisotropic α-Mn_2O_3 channeled N-doped rGO nanosheets. *In situ* generated α-Mn_2O_3 nanocrystals were highly dispersed on N-doped GO nanosheets and directed by N-doped rGO to grow along the direction perpendicular to specific facet simultaneously. Two kinds of coordination structures were formed between N-doped rGO nanosheets and α-Mn_2O_3 nanocrystals. On the one hand, generation of Mn-O-C bond during cross-linking process greatly strengthened the stability of membranes for a long-term operation. On the other hand, because of spatial confinement effects and high binding energy between central Mn and N atoms, rGO nanosheets with N-containing coordinated links were desirable supports to construct numerous Mn-N-C bonds and thus generated artificial nanopores to significantly increase the nanochannels for ultrafast mass transport. The prepared dual-metal-coordinated ultrathin Mn/N-rGO nanofilms achieved ultrahigh permeance up to 210 L m^{-2} h^{-1} bar^{-1} together with very competitive rejection of 99.8% for small organic molecules, superior to the most reported GO-based and polymeric ultrathin nanofiltration membranes. The anticipated nanofilms made by manipulating the types and characters of metal centers and corresponding coordination atoms are very promising in practical applications including catalysis, energy storage, biopharmaceutical, optics, and sensors. Given the overall significance of tunable ultrathin GO-based materials for a diverse range of molecular sieving and chemical conversion, the ultrathin nanofilm-processing approach described here may overcome major limitations of state-of-the-art processes and serve as basic approach to create scalable 2-dimensional ultrathin membranes with outstanding performance.

Limitations of the study

Until now, it is very difficult to quantitatively evaluate the friction of liquid through the membranes by characterizations. Although theoretical models were established to qualitatively describe the separation behavior, more desirable theoretical models are needed for quantitatively illustrating the mass transfer resistance during filtration.

STAR★METHODS

Detailed methods are provided in the online version of this paper and include the following:

- KEY RESOURCES TABLE
- RESOURCE AVAILABILITY
  - Lead contact
  - Materials availability
  - Data and code availability
- EXPERIMENTAL MODEL AND SUBJECT DETAILS
- METHOD DETAILS
  - Synthesis of graphene oxide
  - Synthesis of PSF support
  - Synthesis of single- and dual-metal-coordinated Mn/N-rGO nanofilms
  - Characterization
  - Experiments on pure water flux and dyes rejection
  - Soaking tests of prepared membranes
  - Molecular dynamics simulations
- QUANTIFICATION AND STATISTICAL ANALYSIS
- ADDITIONAL RESOURCES

SUPPLEMENTAL INFORMATION

Supplemental information can be found online at https://doi.org/10.1016/j.isci.2021.102576.

ACKNOWLEDGMENTS

We thank Prof. Z.Q. Tian for useful discussions and Dr. R. Hou, M. Yin, Z.X. Fan and Prof. J.Z. He for technical assistance. This work was supported by the National Natural Science Foundation of China (No. 21736009 and 21808202), the Zhejiang Provincial Bureau of Science and Technology, China (Grants No. 2021C03169), SINOPEC Science and Technology Development Project from China Petrochemical Corporation (No.33750000-20-ZC0607-0012) and Tongjiang Scholarship from Fujian Quanzhou Government.

AUTHOR CONTRIBUTIONS

Z.X., Y.Z., and G.Z. conceived of the concept. Z.X., Y.Z., and X.Z. synthesized the nanocrystal materials and nanofilms and developed related models. Z.X., Y.Z., X.Z., Y.J.Z., C.S., and Y.L. carried out related characterizations and measurements and analyzed the data. Q.M. and C.G. contributed to the general methodology and reviewed the manuscript. G.Z. supervised the project, helped design the experiments and co-drafted the manuscript. All authors contributed to the analysis of the manuscript.

DECLARATION OF INTERESTS

The authors declare no competing interests.

Received: February 16, 2021
Revised: May 10, 2021
Accepted: May 18, 2021
Published: June 25, 2021

REFERENCES

Che-Ning Yeh, K.R., Shao, J., Yang, Q.H., and Huang, J. (2015). On the origin of the stability of graphene oxide membranes in water. Nat. Chem. *7*, 166–170.

Cohen-Tanugi, D., and Grossman, J.C. (2012). Water desalination across nanoporous graphene. Nano Lett. *12*, 3602–3608.

Fane, A.G., Wang, R., and Hu, M.X. (2015). Synthetic membranes for water purification: status and future. Angew. Chem. Int. Ed. *54*, 3368–3386.

Fathizadeh, M., Tien, H.N., Khivantsev, K., Chen, J.T., and Yu, M. (2017). Printing ultrathin graphene oxide nanofiltration membranes for water purification. J. Mater. Chem. A *5*, 20860–20866.

Karan, S., Jiang, Z.W., and Livingston, A.G. (2015). Sub-10 nm polyamide nanofilm with ultrafast solvent transport for molecular separation. Science *348*, 1347–1351.

Ko, T., Kim, K., Lim, M., Nam, S.Y., Kim, T., Kim, S., and Lee, J. (2015). Composite membranes having poly(2,5-benzimidazole)-grafted graphene oxide for fuel cell applications. J. Mater. Chem. A *3*, 20595–20606.

Li, H., Song, Z., Zhang, X., Huang, Y., Li, S., Mao, Y., Ploehn, H.J., Bao, Y., Yu, M., and Ultrathin. (2013). molecular-sieving graphene oxide membranes for selective hydrogen separation. Science *342*, 95–98.

Li, W., Zhang, Y., Xu, Z., Meng, Q., Fan, Z., Ye, S., and Zhang, G. (2016a). Assembly of MOF microcapsules with size-selective permeability on cell walls. Angew. Chem. Int. Ed. *55*, 955–959.

Li, W.B., Zhang, Y.F., Su, P.C., Xu, Z.H., Zhang, G., Shen, C., and Meng, Q. (2016b). Metal-organic framework channelled graphene composite membranes for H2/CO2 separation. J. Mater. Chem. A *4*, 18747–18752.

Li, W.B., Zhang, Y.F., Xu, Z.H., Yang, A.S., Meng, Q., and Zhang, G. (2014). Self-assembled graphene oxide microcapsules with adjustable permeability and yolk-shell superstructures derived from atomized droplets. Chem. Commun. *50*, 15867–15869.

Lin, C.E., Zhou, M.Y., Hung, W.S., Zhu, B.K., Lee, K.R., Zhu, L.P., and Fang, L.F. (2018). Ultrathin nanofilm with tailored pore size fabricated by metal-phenolic network for precise and rapid molecular separation. Sep. Purif. Technol. *207*, 435–442.

Liu, L.F., Zhou, Y., Xue, J., and Wang, H.H. (2019). Enhanced antipressure ability through graphene oxide membrane by intercalating g-C3N4 nanosheets for water purification. Aiche J. *65*, e16699.

Ma, H., Xie, Q., Wu, C., Shen, L., Hong, Z., Zhang, G., Lu, Y., and Shao, W. (2019). A facile approach to enhance performance of PVDF-matrix nanocomposite membrane via manipulating migration behavior of graphene oxide. J. Membr. Sci. *590*, 117268.

Mi, B. (2014). Graphene oxide membranes for ionic and molecular sieving. Science *343*, 740–741.

Morelos, G.A., Cruz, S.R., Muramatsu, H., Ortiz, M.J., Araki, T., Fukuyo, T., Tejima, S., Takeuchi, K., Hayashi, T., Terrones, M., and Endo, M. (2017). Effective NaCl and dye rejection of hybrid graphene oxide/graphene layered membranes. Nat. Nanotechnol. *12*, 1083–1088.

Nam, Y.T., Choi, J., Kang, K.M., Kim, D.W., and Jung, H.T. (2016). Enhanced stability of laminated graphene oxide membranes for nanofiltration via interstitial amide bonding. ACS Appl. Mater. Interfaces *8*, 27376–27382.

Nam, Y.T., Kim, S.J., Kang, K.M., Jung, W.B., Kim, D.W., and Jung, H.T. (2019). Enhanced nanofiltration performance of graphene-based membranes on wrinkled polymer supports. Carbon *148*, 370–377.

Noble, R.D. (2006). Overview of "Green" Separation processes. Green Separation Processes: Fundamentals and Applications (John Wiley & Sons, Ltd.).

Park, H.B., Kamcev, J., Robeson, L., Elimelech, M., and Freeman, B. (2017). Maximizing the right stuff: the trade-off between membrane permeability and selectivity. Science *356*, eaab0530.

Petersen, R.J. (1993). Composite reverse osmosis and nanofiltration membranes. J. Membr. Sci. *83*, 81–150.

Riley, R.L. (1991). Reverse osmosis. In Membrane Separation Systems, R.W. Baker, E.L. Cussler, W. Eykamp, W.J. Koros, R.L. Riley, and H. Strathmann, eds. (Noyes Data Corp), pp. 107–110.

Shannon, M.A., Bohn, P.W., Elimelech, M., Georgiadis, J.G., Mariñas, B.J., and Mayes, A.M. (2008). Science and technology for water purification in the coming decades. Nature *452*, 301–310.

Shen, J., Liu, G., Huang, K., Chu, Z., Jin, W., and Xu, N. (2016). Subnanometer two-dimensional graphene oxide channels for ultrafast gas sieving. ACS Nano *10*, 3398–3409.

Shen, J.L., Zhang, R.N., Su, Y.L., Shi, B.B., You, X., Guo, W.X., Ma, Y., Yuan, J.Q., Wang, F., and Jiang, Z.Y. (2019). Polydopamine-modulated covalent organic framework membranes for molecular separation. J. Mater. Chem. A *7*, 18063–18071.

Song, X., Zambare, R.S., Qi, S., Nil, B.S., Selvaraj, A.P.J., Tang, C.Y., and Gao, C. (2017). Charge-gated ion transport through polyelectrolyte intercalated amine reduced graphene oxide membranes. ACS Appl. Mater. Interfaces *9*, 41482–41495.

Soyekwo, F., Zhang, Q.G., Gao, R.S., Qu, Y., Lin, C.X., Huang, X.L., Zhu, A.M., and Liu, Q.L. (2017). Cellulose nanofiber intermediary to fabricate highly-permeable ultrathin nanofiltration membranes for fast water purification. J. Membr. Sci. *524*, 174–185.

Sun, Z., Wu, Q., Ye, C., Wang, W., Zheng, L., Dong, F., Yi, Z., Xue, L., and Gao, C. (2019). Nanovoid membranes embedded with hollow zwitterionic nanocapsules for a superior desalination performance. Nano Lett. *19*, 2953–2959.

Tan, Z., Chen, S., Peng, X., Zhang, L., and Gao, C. (2018). Polyamide membranes with nanoscale Turing structures for water purification. Science *360*, 518–521.

Vankelecom, I.F.J. (2002). Polymeric membranes in catalytic reactors. Chem. Rev. *102*, 3779–3810.

Wang, J., Yuan, Z., Wu, X., Li, Y., Chen, J., and Jiang, Z. (2019a). Beetle-inspired assembly of heterostructured lamellar membranes with polymer cluster-patterned surface for enhanced molecular permeation. Adv. Funct. Mater. *29*, 1900819.

Wang, Q.M., Zhao, G.J., Li, C.X., and Meng, H. (2019b). Orderly stacked ultrathin graphene oxide membranes on a macroporous tubular ceramic substrate. J. Membr. Sci. *586*, 177–184.

Wang, T., Wang, Q., Wang, Y., Da, Y., Zhou, W., Shao, Y., Li, D., Zhan, S., Yuan, J., and Wang, H. (2019c). Atomically dispersed semi-metallic selenium on porous carbon membrane as an electrode for hydrazine fuel cells. Angew. Chem. Int. Ed. *58*, 13466–13471.

Wang, Y., Li, L., Wei, Y., Xue, J., Chen, H., Ding, L., Caro, J., and Wang, H. (2017). Water Transport with ultralow friction through partially exfoliated g-C3N4 nanosheet membranes with self-supporting spacers. Angew. Chem. Int. Ed. *56*, 8974–8980.

Williams, M.E., Bhattacharyya, D., Ray, R.J., and McCray, S.B. (1992). Selected applications. In Membrane Handbook, W.S.W. Ho and K.K. Sirkar, eds. (Van Nostrand Reinhold), pp. 312–315.

Wu, W., Zhang, X., Qin, L., Li, X., Meng, Q., Shen, C., and Zhang, G. (2020). Enhanced MPBR with polyvinylpyrrolidone-graphene oxide/PVDF hollow fiber membrane for efficient ammonia nitrogen wastewater treatment and high-density Chlorella cultivation. Chem. Eng. J. *379*, 122368.

Xu, W.L., Fang, C., Zhou, F., Song, Z.N., Liu, Q.L., Qiao, R., and Yu, M. (2017). Self-Assembly: a facile way of forming ultrathin, high-performance graphene oxide membranes for water purification. Nano Lett. *17*, 2928–2933.

Xu, X.L., Lin, F.W., Du, Y., Zhang, X., Wu, J., and Xu, Z.K. (2016). Graphene oxide nanofiltration membranes stabilized by cationic porphyrin for high salt rejection. ACS Appl. Mater. Interfaces *8*, 12588–12593.

Xu, Y.Q., Wu, M.Y., Yu, S.Y., Zhao, Y., Gao, C.J., and Shen, J.N. (2019). Ultrathin and stable graphene oxide film via intercalation polymerization of polydopamine for preparation of digital inkjet printing dye. J. Membr. Sci. *586*, 15–22.

Yang, H., Chen, X., Chen, W., Wang, C., Cuello, N., Nafady, A., Al-Enizi, A.M., Waterhouse, G.I.N., Goenaga, G.A., Zawodzinski, T.A., et al. (2019a). Tunable synthesis of hollow metal-nitrogen-carbon capsules for efficient oxygen reduction catalysis in proton exchange membrane fuel cells. ACS Nano *13*, 8087–8098.

Yang, Q., Su, Y., Chi, C., Cherian, C.T., Huang, K., Kravets, V.G., Wang, F.C., Zhang, J.C., Pratt, A., Grigorenko, A.N., et al. (2017). Ultrathin graphene-based membrane with precise molecular sieving and ultrafast solvent permeation. Nat. Mater. *16*, 1198–1202.

Yang, Y., Yang, X., Liang, L., Gao, Y., Cheng, H., Li, X., Zou, M., Cao, A., Ma, R., Yuan, Q., and Duan, X.F. (2019b). Large-area graphene-nanomesh/carbon-nanotube hybrid membranes for ionic and molecular nanofiltration. Science *364*, 1057–1062.

You, X.D., Wu, H., Zhang, R., Su, Y.L., Cao, L., Yu, Q.Q., Yuan, J.Q., Xiao, K., He, M., and Jiang, Z.Y. (2019). Metal-coordinated sub-10 nm membranes for water purification. Nat. Commun. *10*, 4160.

Yu, M., Wang, L., Liu, J., Li, H., Lang, X., Zhao, C., Hong, Z., and Wang, W. (2019). Sponge effect boosting oxygen reduction reaction at the Inter. between mullite SmMn2O5 and nitrogen-doped reduced graphene oxide. ACS Appl. Mater. Interfaces *11*, 17482–17490.

Zhang, C., and Koros, W.J. (2017). Ultraselective carbon molecular sieve membranes with tailored synergistic sorption selective properties. Adv. Mater. *29*, 1701631.

Zhang, M., Guan, K., Ji, Y., Liu, G., Jin, W., and Xu, N. (2019). Controllable ion transport by surface-charged graphene oxide membrane. Nat. Commun. *10*, 1253.

Zhang, Y., Zhang, S., and Chung, T.S. (2015). Nanometric graphene oxide framework membranes with enhanced heavy metal removal via nanofiltration. Environ. Sci. Technol. *49*, 10235–10242.

Zhao, Y., Zhou, C., Wang, J.Q., Liu, H.W., Xu, Y.Q., Seo, J.W., Shen, J.N., Gao, C.J., and Van der Bruggen, B. (2018). Formation of morphologically confined nanospaces via self-assembly of graphene and nanospheres for selective separation of lithium. J. Mater. Chem. A *6*, 18859–18864.

Zhang, Y.F., Xu, Z.H., Zhang, T.T., Meng, Q., Zhang, X., Shen, C., Lu, Y.H., Zhang, G., and Gao, C.J. (2020). Self-assembly of robust graphene oxide membranes with chirality for highly stable and selective molecular separation. J. Mater. Chem. A. *8*, 16985–16993.

STAR★METHODS

KEY RESOURCES TABLE

REAGENT or RESOURCE	SOURCE	IDENTIFIER
Chemicals and materials		
sodium borohydride	Aladdin	CAS: 7631-99-4
levodopa	Aladdin	CAS: 59-92-7
manganous nitrate tetrahydrate	Aladdin	CAS: 20694-39-7
manganese sulfate tetrahydrate	Aladdin	CAS: 10101-68-5
manganese acetate	Aladdin	CAS: 6156-78-1
cobalt nitrate hexahydrate	Aladdin	CAS: 10026-22-9
ferric nitrate nonahydrate	Aladdin	CAS: 7782-61-8
hydrochloric acid	Shanghai Sinopharm Chemical	CAS: 7647-01-0
1-methyl-2-pyrrolidone	Aladdin	CAS: 872-50-4
trismetyl aminomethane hydrochloride	Aladdin	CAS: 1185-53-1
$KMnO_4$	Shanghai Sinopharm Chemical	CAS: 7722-64-7
$NaNO_3$	Shanghai Sinopharm Chemical	CAS: 7631-99-4
H_2SO_4	Shanghai Sinopharm Chemical	CAS: 7664-93-9
H_2O_2	Shanghai Sinopharm Chemical	CAS: 7722-84-1
graphite flakes (500 mesh)	XF Nano	CAS: 7782-42-5
polysulfone	Shuguang Chemical	CAS: 25154-01-2
methylene blue	Aladdin	CAS: 61-73-4
methyl orange	Aladdin	CAS: 547-58-0
rhodamine B	Aladdin	CAS: 81-88-9
reactive brilliant red	Betapharma	CAS: 17804-49-8
methyl green	Aladdin	CAS: 7114-03-6
congo red	Aladdin	CAS: 573-58-0
methyl blue	Aladdin	CAS: 28983-56-4
naphthol green B	Aladdin	CAS: 19381-50-1
evans blue	Aladdin	CAS: 314-13-6
Software and algorithms		
Materials Studio software	Accelrys Incorporation	N/A
Nano measurer software	Analytical Software Website	https://www.jb51.net/softs/583257.html

RESOURCE AVAILABILITY

Lead contact

Further information and requests for resources should be directed to the lead contact, Guoliang Zhang (guoliangz@zjut.edu.cn).

Materials availability

This work did not generate new unique reagents.

Data and code availability

The data are available upon request by contacting lead contact, Guoliang Zhang (guoliangz@zjut.edu.cn). No new code was generated during the course of this study.

EXPERIMENTAL MODEL AND SUBJECT DETAILS

Any animals, human subjects, plants, microbe strains, cell lines, or primary cell cultures were not used in the study.

METHOD DETAILS

Synthesis of graphene oxide

Graphene oxide was prepared by improved Hummer's method (Li et al. 2014). First, 2 g natural graphite flakes (500 mesh) and 1 g $NaNO_3$ were dispersed into 46 mL of concentrated H_2SO_4 in an ice bath and 6 g $KMnO_4$ was added into the suspension under stirring to prevent temperature from exceeding 20 °C. The suspension was kept in an ice bath for 2 h, and then, it was heated to 35 °C in a thermostatic bath in which it was maintained for 1 h. Later, 92 mL of water was slowly poured into the mixture. The suspension was kept at 98 °C for 40 min. After cooling, the mixture was treated with H_2O_2 (30 wt%) solution. Finally, the product was washed with diluted HCl solution, collected, and dried at 80 °C overnight.

Synthesis of PSF support

In a typical process (Williams et al., 1992), 3.53 g of PSF powder was dispersed in 20 mL 1-methyl-2-pyrrolidone. Then, casting solution was stirred for 12 h and sonicated for 1 h and kept standing for 6 h to more air bubbles. After that, dope solution was placed on a glass plate and cast by using a 200-μm-thick casting knife. The glass plate was then put in a nonsolvent bath. After phase separation and membrane formation, the prepared 200-μm PSF support was preserved in deionized water.

Synthesis of polylevodopa-coated PSF support. In a typical process, 1 mmol trismetyl aminomethane was added to 100 mL deionized water and sonicated to dissolve. Then, the solution was adjusted to pH = 8.5 by using 0.1 M HCl. 0.2 g levodopa was added to the solution and sonicated to dissolve. Finally, PSF support was put into the solution for 24 h. After the process was over, the polylevodopa-coated support was washed by deionized water to remove liquid surface residual.

Synthesis of single- and dual-metal-coordinated Mn/N-rGO nanofilms

The dual-metal-coordinated Mn/N-rGO nanofilms were synthesized by assembling Mn_2O_3 nanocrystals channeled N-doped reduced graphene oxide nanosheets (Mn/N-rGO) on polylevodopa (PLDA)-coated polymer supports. Unlike conventional metal-coordinated N-doped carbon compounds, here, metal/N-rGO building blocks were constructed via a facile and low-cost one-step coordination-aided chemical etching method, no need for high-temperature pyrolysis. Typically, a specified volume of narrow-dispersed graphene oxide (1 g/L) was dispersed in 50 mL deionized water to make uniformly dispersed solution. By controlling the content of nitrogen, a certain amount of manganous nitrate was added dropwise into the graphene oxide solution. After ultrasonic treatment, 0.1 M $NaBH_4$ was added into the solution and sonicated for 30 min. The mixed solution with a controllable volume was filtrated onto the PLDA-coated PSF support. Then, the membrane was dried at 60 °C and kept in water. Meanwhile, the single-metal-coordinated Mn/rGO nanofilm was prepared by a similar strategy by using manganese sulfate and manganese acetate as precursors and filtrated onto the pure PSF support.

Characterization

The surface morphology of the prepared samples was evaluated by Hitachi JEM-1200EX transmission electron microscopy (Hitachi, Japan), JEM-2100 transmission electron microscopy (Jeol, Japan), and Tecnai G2 F30 S-Twin high-resolution transmission electron microscopy (Philips-FEI, Holland). Fourier Transform Infrared (FTIR) spectrophotometers of the samples were recorded by the KBr disk technique with a Nicole 6700 Fourier transform infrared spectrometer (Thermo, USA). The X-ray diffraction of the nanocomposites was determined by an X'Pert PRO X-ray diffractometer (PNAlytical, Cu Kα radiation). Nitrogen adsorption-desorption isotherms were obtained by an ASAP 2020 surface area and porosity analyzer (Micromeritics, USA) at 77 K. Energy-dispersive spectroscopy (Hitachi, S-3700N, Japan) was used for the composition detection of different samples. The X-ray photoelectron spectroscopy experiments were carried out on an RBD upgraded PHI-5000C ESCA system (Perkin Elmer) with Mg K radiation (h=1253.6eV), and binding energies were calibrated by using the containment carbon (C1s=284.6eV). The contact angle was measured by a contact-angle-measuring instrument (Germany, DataPhysics). The atom force microscope was carried out on a Brucker Dimension Icon. The ultraviolet and visible spectrum (UV) was measured by UV1120 (Hitachi). The mechanical properties of prepared pure GO and Mn/N-rGO films with a thickness of 500 nm were measured by nanoindentation test equipped with a Nano-indenter G200 at room temperature. The content of Mn leached from prepared membrane was analyzed by ICP-MS in an Optima 2000 instrument (PerkinElmer, USA).

Experiments on pure water flux and dyes rejection

Both experiments were carried out with an effective membrane area of 7.065 cm^2. The cross-flow rate was 90 L h^{-1} with a rotameter which corresponded to a flow velocity of 31.35 cm s^{-1} and a Reynolds number of 1892. In a typical process, water flux was measured by recording the time receiving a certain volume of deionized water in room temperature. Then, we used the equation to calculate the flux:

$$F=\Delta V/(\Delta P*S*T)$$

where ΔV is a certain volume of solution, S is the effective filtration area, ΔP is the operation pressure, and T is the time receiving a certain volume of solution. In our experimental process, ΔV is 2 mL and S is 7.065 cm^2.

Rejection of dyes (50 mg/L) was measured by a UV spectrophotometer. The formula is as follow:

$$R(\%) = \left(1 - \frac{C_p}{C_f}\right) \times 100$$

where R is the dye rejection ratio (%), C_p is the dye concentration of the permeate (g/L), and C_f is the dye concentration of the feed (g/L).

Soaking tests of prepared membranes

The pure GO and prepared Mn/N-rGO nanofilms were soaked in water for a period of time at pH=3, 7, and 10.

Molecular dynamics simulations

To understand the fluid behavior and interactions between Mn/N-rGO composite nanosheets and water molecules, the molecular dynamics simulations were used with the Materials Studio software package from Accelrys Incorporation. The model and force field of N-doped rGO nanosheets and Mn_2O_3 nanoparticles were derived from previous literature. N-rGO nanosheets with a certain amount of oxygen-containing groups and N-doped sites were selected to construct the model by amorphous cell module with the size of 300×180×10.00 Å3. Single-layer composite nanosheets with 1.1-, 1.3-, 1.9-, and 5.9-nm nanopore were built. Water molecules were also modeled with charges in the amorphous cell module. Two and four layers of Mn/N-rGO nanosheets were constructed. Different Mn/N-rGO membranes were filled with water in the simulation box with the Forcite module, yielding a simulation system containing 2000 molecules. The time step was set as 1.0 fs, and the COMPASS force field was used with the Berendsen algorithm to maintain a constant temperature (298 K) and pressure (80 kPa). Energy minimization method was used to optimize the atomistic structures for 120000 steps so as to eliminate the local nonequilibrium, and then, 12000-ps NVT equilibrium simulation runs were carried out to further equilibrate the models. The Mn/N-rGO composite nanosheets were immobilized in simulations because the nanosheets were rather rigid. The number of water molecules passing through the Mn/N-rGO composite nanosheets was counted as the function of simulation time.

QUANTIFICATION AND STATISTICAL ANALYSIS

The thickness of Mn/N-rGO nanofilms was evaluated by Nano Measurer software, and error bars represent standard deviations for at least 5 measurements. Data are presented as mean ± SEM. Moreover, the frequency of size of Mn_2O_3 nanoparticles in different samples was obtained by Nano Measurer software.

ADDITIONAL RESOURCES

There is no additional resources need to be declared in this manuscript, additional requests for this can be made by contacting the lead contact.